ASSESSMENT OF NONLINEAR BOND LAWS FOR NEAR-SURFACE-MOUNTED SYSTEMS IN CONCRETE ELEMENTS

Francesca CERONI*

Assistant Professor

Engineering Department, University of Sannio

Piazza Roma, 21, 82100 - Benevento, Italy, *ceroni@unisannio.it**

Joaquim A.O. BARROS

Full Professor

Department of Civil Engineering, University of Minho

Campus de Azurém, 4800-058 Guimarães, Portugal, *barros@civil.uminho.pt*

Marisa PECCE

Full Professor

Engineering Department, University of Sannio

Piazza Roma, 21, 82100 - Benevento, Italy, *pecce@unisannio.it*

Marco IANNICIELLO

Graduate student

Engineering Department, University of Sannio

Piazza Roma, 21, 82100 - Benevento, Italy*, marcoianniciello@libero.it*

Abstract

This paper presents a numerical plane Finite Element (FE) Model for use in simulating the behaviour of different types of Near Surface Mounted (NSM) Fibre Reinforced Plastic (FRP) strengthening systems for concrete elements. Based on a nonlinear bond law for simulating the behaviour of the FRP reinforcement-adhesive-concrete interface, the model employs an interface element between the NSM FRP reinforcement and the

*Corresponding author
Engineering Department, University of Sannio
Piazza Roma, 21, 82100 - Benevento, Italy
Tel. +39-824-305566, Fax +39-824325246, E-mail: *ceroni@unisannio.it*

concrete. The results of two different experimental programs, both dealing with 'bond tests' but with distinct set-ups, are briefly summarised and analysed. The main objective of this research is to assess the values of the parameters that define the nonlinear bond laws for each type of FRP reinforcement tested. This assessment was accomplished by inverse analysis, fitting numerically the pullout load–displacement curves that were experimentally recorded. The effect of bond length on different types of NSM FRP reinforcement is assessed. Finally, the bond behaviour in the transverse plane is examined too.

Keywords: A. Polymer-matrix composites (PMCs), B. Debonding, B. Fibre/matrix bond, C. Finite Element Analysis, NSM systems.

1. Introduction

Recently, the use of Fibre Reinforced Plastic (FRP) materials for the repair and strengthening of concrete structures has increased due to several advantages of these composites for use as external reinforcement compared to conventional materials and construction systems, such as externally bonded steel plates, steel or concrete jackets and external post-tensioning (CSA [1]; JSCE [2]; fib bulletin [3]; CNR DT 200 [4]; ACI 440 [5]). One of the main design issue in using FRP plates or sheets that have been externally bonded to concrete elements is the well-known phenomenon of debonding of the reinforcement from the concrete substrate, which is a typical failure mode of this strengthening system and precludes the exploitation of the high tensile strength of the fibres (Smith and Teng [6]; Ceroni and Pecce [7]).

A more recently developed technique, designated as Near Surface Mounted (NSM)

reinforcement, has been shown to be very effective for flexural (Barros and Fortes, 2005) and shear (Dias and Barros [8]) strengthening of concrete elements, because the tensile capacity of FRP systems is more effectively mobilised. NSM systems are composed of FRP bars or strips that are installed in grooves cut into the concrete cover of the element to be strengthened (De Lorenzis and Nanni [9]; Blaschko and Zilch [10]. Several researchers have investigated the NSM technique, executing experimental tests to assess its capabilities in terms of load-carrying capacity (De Lorenzis and Nanni [9]; De Lorenzis and Teng [11]; Sena Cruz and Barros [12]; Hassan and Rizkalla [13]; Seracino et al. [14]; Bilotta et al. [15]; Novidis and Pantazopoulou [16]; Borchert and Zilch [17]; Encore & fib reports [18]). The experimental results show that the load-carrying capacity of NSM systems is strongly influenced by the bond behaviour, which is dependent on: the mechanical properties of the FRP reinforcement, the groove filler and the concrete substrate, the surface properties of the FRP reinforcement and of the grooves, the shape of the strengthening system (bars or strips), the dimensions of the groove and the depth of the FRP reinforcement in the groove (De Lorenzis and Nanni [9]; De Lorenzis and Teng [11]; Sena Cruz and Barros [12]; Seracino et al. [14]).

The objective of this research is the assessment of the values of the parameters of a bond stress–slip law, τ–s, for the modelling of the interface behaviour between NSM FRP bars/strips and concrete, using a Finite Element Model (FEM). Using the general τ–s law proposed by Sena Cruz et al., [19], the pullout bond tests conducted by Bilotta et al. [15] and Macedo et al. [20] on concrete blocks where different types of FRP NSM systems were installed, were simulated with a FE model. Some of the experimental results are summarised herein. The strain field in the FRP NSM reinforcement, the shear stresses along the FRP-concrete interface, and the tensile stresses in the concrete

surrounding the FRP reinforcement were determined numerically. By fitting the global pullout force–displacement curves recorded in the experimental tests, the values of the parameters of the bond law were determined for each NSM system tested.

2. Synthesis of the experimental results

2.1 Experimental programs

As previously introduced, the numerical studies presented in this paper are based on the experimental results of two different programs on bond tests carried out by the authors (Bilotta et al. [15]; Macedo et al. [20]). The meaningful data obtained from the two programs, designated as Programs 1 and 2, are herein presented and discussed briefly .The specimens tested in Program 1, described in detail in (Bilotta et al. [15]), are made of prismatic concrete blocks (dimensions b_c = 160 mm, h_c = 200 mm, L_c = 400 mm) where glass, basalt and carbon FRP bars or carbon FRP strips were installed into longitudinal grooves (NSM technique,Figure 1). Four different types of bar and a strip were considered, and three equal specimens have been prepared and tested for each type of FRP. NSM reinforcement was embedded in a groove longitudinally cut into the cover of the prisms after concrete hardening (Figure 1). The experimental arrangement is an asymmetrical 'pull–pull' test, wherein the FRP reinforcement is pulled by the upper grips of an universal testing machine, while the concrete block is fixed to the lower grips of the same machine by means of a pair of internal steel bars connected with bolts to a stiff steel plate (see Figure 1). This configuration introduces a tensile load in the concrete block. To reuse each specimen as much as possible, the NSM systems were applied on two lateral faces of the concrete block so that two pullout tests could be conducted on each

specimen. The same bond length was used for all of the specimens (L_b = 300 mm). Five strain gauges, spaced 70 mm apart, have been glued onto the surface of each NSM bar or strip before the adhesive was applied and the reinforcement was placed into the groove.

The main test variables were the following: the type of reinforcement (bars or strips), the type of fibres (glass, basalt, or carbon), Young's modulus (46 to 182 GPa), the diameter of the bars (d = 6 or 8 mm), and the surface treatments of the bars. The following combinations of bar fibre type, diameter, and surface treatment were used: sand-coated round basalt bars 6 and 8 mm in diameter (B-6-SC and B-8-SC), ribbed round glass bars 8 mm in diameter (G-8-RB), smooth round carbon bars 8 mm in diameter (C-8-S), and smooth carbon strips 2.5 mm thick and 15 mm wide (C-2.5x15-S). The 6- and 8-mm-diameter bars were placed into square grooves 10 and 14 mm on a side, respectively; the strips were placed in grooves with rectangular cross-sections of 25 mm x 8 mm. The groove shape factor, k, is defined as the ratio between the groove width and the bar diameter or strip width and is always greater than 1.5. This is the minimum value suggested to avoid splitting failure of the epoxy (De Lorenzis and Teng [11]).

Epoxy adhesive was used to affix the bars and the strips into the grooves.

The notation of specimens is A-x-B-n, where A refers to the reinforcement material (B, G, or C for Basalt, Glass or Carbon), x identifies the bar diameter or strip thickness and width (6 or 8 mm for the round bars and 2.5x15 for the strips), B denotes the surface treatment ("SC" for Sand-Coating, "S" for Smooth, "RB" for RiBbed), and n distinguishes the ordinal number of tests (1, 2 or 3).

All of the specimens have been cast in a single batch. The mean cylinder concrete compressive strength at 28 days after casting was f_{cm} = 19 MPa, and the mean Young's modulus, E_c, was 18.6 GPa. At the time of the bond tests (about 200 days after casting), the mean cubic compressive strength was 23.1 MPa. The average tensile strength, f_{ctm}, was estimated to be 2.0 MPa (Eurocode 2 [21]). The low values of these mechanical properties are due to the chosen concrete mixture, designed to simulate poor-quality concrete in an existing building.

In experimental Program 2, described in detail in (Macedo et al. [20]), the bond tests were conducted on concrete blocks where smooth carbon FRP strips (cross-section of 1.4 mm by 10 mm, C-1.4x10-S) were inserted in grooves. The experimental arrangement was an asymmetrical pullout configuration in which the NSM strips were loaded in tension and the concrete block was compressed (see Figure 2). The specimens had dimensions of 150 mm x 150 mm x 600 mm, and several bond lengths (40, 70, 90, 120, and 150 mm) were tested. The strips were placed in a groove with rectangular cross section of 22 mm x 5 mm. Thus, the minimum shape factor k was 2.2. For each value of L_b, two specimens were prepared to test the effect of the position of the strip in the groove; two positions were considered and identified by the distance, x_i, of the strip from the top (6 and 12 mm, as shown in Figure 2). Epoxy adhesive was used to affix the strips in the grooves.

One displacement transducer (LVDT1) was used to measure the displacement between the left edge of concrete specimen (*section 0*) and the first FRP point bonded to concrete (*section 1*). This displacement is hereafter referred to as the displacement at the loaded end, d_l. A second displacement transducer (LVDT2) was used to measure the displacement at the free end, d_{fr}, i.e., the displacement between the last FRP bonded

point (*section 2*) and the concrete point located at *section 3*. Strain gauges were also glued on the strip to estimate the strain variation in the bonded region. The notation used for the series of tests is *LbY_xZ*, where *Y* and *Z* are the CFRP bond length (40, 70, 90, 120 or 150 mm) and its position in the groove (6 or 12 mm), respectively.

The mean cylinder compressive strength, f_{cm}, at 28 days after casting was25 MPa, and the mean Young's modulus, E_c, was 29 GPa. Based on the Eurocode 2 [21], the average tensile strength, f_{ctm}, was estimated to be 2.6 MPa.

2.2 **Experimental results**

For each NSM system tested in Programs 1 and 2, Tables 1 and 2 show the following relevant results: the ultimate tensile strength f_{fu}, the Young's modulus E_f, the axial stiffness E_f A_f , the groove shape factor k, the failure mode, the maximum load F_{max}, and the loaded-end slip at F_{max}, d_{max}. The mechanical properties of the FRP are the average values obtained from experimental tensile tests with five specimens, according to (ASTM-D3039, 2000).

In Program 1, the displacements *d* were calculated by integrating the measures of strain along the bonded length, while in Program 2 they were determined directly as the difference between the LVDT1 measure, d_l, and the elastic elongation of the unbonded part of the FRP strip.

In Program 1, bond failure occurred along the epoxy–concrete interface with a layer of concrete attached to the reinforcement for all specimens (see Figure 3a). In Program 2, splitting of the epoxy occurred in all specimens (see Figure 3b), despite the high values of the shape factor, k.

In Program 1, the values of axial stiffness of the NSM reinforcements are quite

dissimilar, ranging between 1300 and 7787 kN. The axial stiffness of the carbon strips tested in Program 2 (2184 kN) is comparable to the stiffness of the 8-mm-diameter basalt bar tested in Program 1 (2311 kN).

3. Numerical analysis

3.1 The FEM model

Numerical simulations were conducted with *FEMIX v4.0*, an FEM-based computer program that can be used for nonlinear analysis of materials. Several constitutive models for cement-based materials, steel and composites can be implemented in FEMIX (Sena Cruz et al. [19]). Both of the test configurations described previously were modelled as plane stress problems.

To simulate the boundary conditions of the specimens tested in Program 1 (Figure 4), the the displacements in direction 3 were set to zero for the nodes of the inferior part of the specimen, as well as the displacement in direction 2 for the nodes of the symmetry axis.

To simulate as closely as possible the support conditions of the specimens tested in Program 2, the top side of the specimen was restrained to prevent displacement in direction 3 and two supports were placed at the lateral faces to prevent displacement in direction 2 at these points (Figure 5).

In both cases, due to the symmetric conditions of the test configurations, only half of each specimen was modelled.

Four-node Lagrangian plane stress elements with a 2×2 Gauss–Legendre integration scheme were used to simulate both the concrete and the FRP NSM reinforcement. The

FRP reinforcement and the concrete were modelled as linear elastic materials, with the Young's modulus values determined in the experimental characterization tests (see Table 1 and 2), and Poisson's ratios of 0.2 for concrete and 0.0 for the FRP reinforcements. Since adopting values of Poisson's ratio available in the literature for the FRP materials has negligible influence on the results of the simulations performed, it was decided to assume a null value for this parameter.

The adhesive was simulated by four-node line interface finite elements with a two-point Lobatto integration rule. The tangential stiffness of the constitutive law of these interface elements is defined once the values of the parameters that define the local τ - s bond law are known. A constant value of 1.0e+06 N/mm^3 was used for the normal stiffness.

The load was applied at two points, and the arc length method was applied by controlling the displacement at the loaded end of the FRP reinforcement, imposing a displacement increment of 0.01 mm in direction 3 (Figure 4b and 5b).

3.2 **The bond law of the interface finite element**

In this study, the determination of the local bond stress–slip relationship for both strips and bars is based on the approach described by Sena Cruz and Barros [11]. Thus, the nonlinear bond law, $\tau - s$, adopted in the FE model is composed of the following three branches:

$$\begin{array}{lll} \tau(s) = m_{lin} \cdot s & \tau(s) = \tau_{\max}\left(\frac{s}{s_{\max}}\right)^{\alpha} & \tau(s) = \tau_{\max}\left(\frac{s}{s_{\max}}\right)^{-\alpha'} \\ \text{if} \quad s \le s_{\lim} & \text{if} \quad s_{\lim} \le s \le s_{\max} & \text{if} \quad s > s_{\max} \end{array} \qquad (1)$$

where τ_{max} is the shear bond strength and s_{max} is the corresponding slip; α and α' are parameters defining the shape of the pre- and post-peak branches, respectively; and m_{lin} represents the initial stiffness of the bond law, assumed to be linear up to a slip of $s_{\lim}$ (Figure 6a). The shape of the pre- and post-peak branches is assumed to be nonlinear. The bond law is fully identified by five parameters, and their significance to the global bond behaviour of concrete elements, where different types of FRP NSM systems were installed, was investigated as described below. The post-peak softening branch of the bond law can tend asymptotically toward a residual or a zero shear stress. The influence of the three branches of the local bond law (ascending linear, ascending nonlinear, and nonlinear softening) on the global pullout relation of a specimen tested in a bond test is represented in Figure 6b. In particular, the maximum force is theoretically reached when the displacement at the loaded end attains the value corresponding to the residual or zero value of shear stress. The bonded length corresponding to these bond conditions is considered the effective bonded length since it guaranties the application of the maximum pullout force. Moreover, the slip corresponding to this condition is defined as the ultimate one, s_{ult}.

3.3 **The influence of bond law parameters on the pullout load**

Parametric numerical analyses conducted using the FE model described in 3.1 and applied to concrete specimens with carbons strips according to the scheme shown in Figure 4 demonstrate that, among the five parameters defining the bond law, the following ones have a significant influence on the global behaviour:

- the peak value of the bond stress–slip curve, τ_{max}, and its corresponding slip, s_{max}; and

- the parameter that defines the shape of the post-peak branch of the $\tau - s$ relationship, α'.

The effect of each of these parameters on the global behaviour is identified as the maximum pullout force, F_{max}, that can be applied to the FRP reinforcement. Note that both the maximum pullout force, F_{max}, and the ultimate displacement, s_{ult}, of the bond law are results of the numerical procedure solving the differential equations of bond. As previously explained, s_{ult} is the value corresponding to the maximum force that is attained when the descending branch of global P-d curve starts (see Figure 6a and 6b).

In Figure 7, the ratio F_{max}/F^0_{max} is plotted against the parameter ξ, which is given by the following three different expressions according to the parameter of the bond law varied in the parametric analyses :

$$\xi = \frac{s_{\max}}{s^0_{\max}} = \frac{\tau_{\max}}{\tau^0_{\max}} = \frac{\alpha'}{\alpha'^0} \tag{2}$$

where $s^0_{\max}$, $\tau^0_{\max}$ and α'^0 represent the minimum values of $s_{\max}$, $\tau_{\max}$ and α' used in the parametric studies, respectively (i.e., $s^0_{\max}$ = 0.08 mm, $\tau^0_{\max}$ = 1.25 MPa and α'^0 = 0.20), and $F^0_{\max}$ is the maximum numerical pullout force for these values. The influence of the other two parameters, s_{lin} and α, on F_{max} was observed to be very low (less than 6% for s_{lin} between 0.03 and 0.30 mm and for α between 0.20 and 1.60) so that in all of the parametric analyses represented in Figure 7, they have been assumed to be equal to 0.05 mm and 0.40, respectively. Figure 7 shows that the most significant parameter that affects the maximum pullout force is the bond strength, τ_{max}. In fact, for $\xi = \frac{s_{\max}}{s^0_{\max}} = \frac{\tau_{\max}}{\tau^0_{\max}} = \frac{\alpha'}{\alpha'^0} = 8$, the values of the $F_{\max} / F^0_{\max}$ ratio are approximately 5, 2, and

0.5, respectively. The significant effect of τ_{max} on the global strength was demonstrated by Ceroni et al. [22] too, even when a simplified bilinear bond law was assumed.

4. Experimental–numerical comparison

4.1 Inverse analysis

The differential equation of bond was solved for some of the specimens tested by Bilotta et al. [15] and Macedo et al. [20], assuming the general bond laws given by Eq. (1).

For the specimens tested in Program 1, the maximum bond stress, τ_{max}, was assessed using the experimental $\tau - s$ relationships obtained on the basis of the strain gauges measurements and considering the experimental average value of equal specimens. In particular, the shear stress was calculated using the measures of the first two strain gauges that were placed at 10 and 80 mm from the loaded end of the FRP reinforcement; thus, the experimental measures refer to the abscissa z = 45 mm (see Figure 4b). The corresponding slip was calculated by integrating the experimental measures of strain along the whole bonded length. Successively, an inverse analysis was performed by determining the values of s_{max} and α' that best fit the experimental pullout force–displacement curves.

In contrast, for the specimens tested in Program 2, the inverse analysis was used directly to assess the values of all of the parameters of the $\tau - s$ relationship because only the slips at the loaded and free ends were measured experimentally.

For the specimens tested in Program 1 the bond shear stresses are referred to the perimeter of the epoxy–concrete interface (because the failure occurred at the epoxy–concrete interface see Figure 8a), while for the specimens tested in Program 2 to the perimeter of the epoxy–FRP reinforcement interface (because a splitting failure of the resin occurred, see Figure 8b). However, the numerical value of maximum pullout force, F_{max}, is independent of the perimeter because the thickness attributed to the interface finite elements that simulate the adhesive is the aforementioned perimeter.

Because the s_{lim} and α parameters have relatively little influence on the *F–d* response (see section 3.3), values of 0.05 or 0.01 and 0.35 or 0.40, respectively, were assumed for these parameters.

In Table 3, the values of the parameters of the bond law assessed for each NSM system are listed for both experimental programs. The numerical and experimental maximum pullout forces ($F_{max,num}$ and $F_{max,exp}$, respectively) are also listed.

In Figure 9, the full numerical and experimental load–displacement curves are compared. Good agreement can be observed, in terms of both the *F–d* curves and the maximum load.

In Figure 10, the experimental $\tau - s$ bond laws derived from the strain gauge measurements and the ones determined from the numerical fitting procedure conducted by the inverse analysis are compared for the carbon strips and the 6-mm-diameter basalt bars tested in Program 1. This type of comparison has been presented for all of the tested specimens by Ianniciello [23]. The graphs demonstrate quite good predictive performance up to the bond strength. The experimental measures are low reliable in the post-peak phase when the damage along the bond length can be significant and, indeed,

were not used for defining the bond law parameters. This confirms that the global behaviour is well captured by the numerical simulations using the inverse analysis approach, while the approach based on local experimental measures is not always reliable.

4.2 **Analysis of the bond behaviour by means of the numerical model**

In Figures 11a–b, the theoretical bond laws assessed for the three types of 8-mm-diameter bars and for the two types of carbon strips are compared, while in Figures 11c–d, the corresponding global *F–d* curves are shown.

In order to compare results of specimens failed in different ways (epoxy-concrete interface failure or epoxy splitting), the bond shear stresses plotted in Figures 11 pertain to the perimeter of the epoxy–concrete interfaces for all specimens of both Programs 1 and 2. These results illustrate the following points:

1) The bond law for the ribbed glass bars has a lower shear strength than that for the sand-coated basalt bars, but a notably lower value of α' makes the post-peak softening branch less brittle (Figure 11a). Moreover, the glass bars are more effective in term of maximum pullout force than the basalt ones (about +50%, see Figure 11c), despite the values of Young's modulus for the two types of bars not being very different (59 GPa vs. 46 GPa). This might be a positive effect of the surface treatment (ribs made of epoxy resin) in the glass bars, while in the case of the basalt bars, only a sand coating is present. In this latter case, the bond law should be, in general, primarily influenced by the cohesion, chemical adhesion and friction phenomena, rather than by interlocking effects that are activated by the presence of ribs along the surface of the glass bars. Thus, for a smooth surface, the post-peak bond behaviour is usually more brittle than for a ribbed surface, due to the rapid decay of bond when the interlocking phenomena

are less pronounced (Eligehausen et al. [24]). However, more testing is necessary to confirm these results, and in this respect, it is important to compare the bond behaviour of bars made of the same materials and dimensions, but with different surface treatments.

2) The smooth carbon bars, with no surface treatment, developed a bond law similar to that of glass bars (Figure 11a), even if they attained a notably smaller ultimate slip (0.9 mm vs. 2.6 mm), which contributed to a less ductile global behaviour of the carbon bars (Figure 11c). The efficiency of the carbon bars is, however, very relevant in terms of failure load, which was the highest one (about 50 kN) within the specimens tested in this experimental program. The relatively high Young's modulus (about 155 GPa) allowed to reach high loads, even if, coupled with the smooth surface of these bars, contributed to make more brittle the global behaviour and have lower ultimate slips in the local bond law.

3) In terms of local behaviour, Young's modulus E_f influences the values of τ_{max} and s_{ult}: in particular, τ_{max} decreases with an increase in E_f, and s_{ult} increases with a decrease in E_f.

4) In terms of global behaviour, as E_f increases, the ultimate displacement reached by the systems, $d_{max,}$ decreases. The initial stiffness of the F–d curves for the 8 mm diameter bars (Figure 11c) also increases with E_f, because this contributes to an increase in the axial stiffness of the FRP system, $E_f \cdot A_f$. In addition, the maximum pullout force, F_{max}, increases with E_f, being A_f equal for the three types of bar.

5) The comparison of the $\tau - s$ of carbon bars and strips of similar E_f and smooth surface tested in Program 1 (Figure 11a and 11b) confirms that the strip type C-2.5x15-S (Figure 11b) developed a bond law of greater s_{max} and s_{ult} compared with the

carbon bars C-8-S, leading to a more ductile response in terms of *F–d* too (Figure 11c and 11d). In particular, the favourable effect of the rectangular shape of the cross-section of the strips is reflected in terms of larger ductility and similar maximum pullout load (mean value approximately 52 kN), despite the smaller axial stiffness of the strips. This can be explained by the larger bond perimeter and the high degree of confinement provided by the surrounding concrete in the case of the strips (Barros and Kotynia [25]).

6) The comparison of the bond law of the two types of carbon strips (one type tested in Program 1 and the other tested in Program 2 and both referred to the epoxy–concrete interface, Figure 11b), reveals that τ_{max} is 8.7 MPa for the C-1.4x10-S strip and 5.2 MPa for the C-2.5x15-S strip. This can be explained by the different geometries of the two strips, which can be characterized by a shape ratio defined as the ratio of the perimeter to the cross-sectional area of the strip, p_{frp}/A_{frp}. For the C-2.5x15-S strip, the ratio p_{frp}/A_{frp} is 0.93, while for the C-1.4x10-S strip, the ratio is 1.63. If p_{frp}/A_{frp} is higher, a larger transfer of shear load is expected: indeed, a larger value p_{frp} means that a larger surface exists for shear transfer, while a smaller value of A_{frp} means a lower axial stiffness that, as already observed for E_f, is indicative of a larger stress transfer. Indeed, in general as the axial stiffness is lower as the strain distribution in the FRP reinforcement are more concentrated and, thus, characterized by lower transfer length; this means higher shear stress close to the loaded end (see the following section 4.3). If the τ_{max} of the C-1.4x10-S strip (8.7 MPa) is scaled by the ratio 0.93/1.63=0.57, a value similar to the τ_{max} of the C-2.5x15-S strip is obtained (approximately 5 MPa). In contrast, the values of the maximum bond stress for the C-2.5x15-S strips and the C-8-S bars, are similar (approximately 5–5.5 MPa), despite the lower value of p_{frp}/A_{frp} (0.5 vs. 0.93) for the bars. However, in this case, the influence of the shape of the NSM

reinforcement (round bar or strip) on the bond behaviour is confirmed because of the different confinement effects of the surrounding concrete that are not taken into account in the simple geometric factor p_{frp}/A_{frp}.

Finally, because the values of the bond parameters of carbon and glass bars tested in Program 1 are relatively similar, the average value for each parameter was determined too. The simulation conducted with these average values for the bond parameters was designated "*global average*" (Table 4) and is represented in Figure 12a, in which the maximum slip reached by the two types of bars is also indicated. In Figures 12b–c, the numerical *F–d* curve obtained using the average bond law is compared with the experimental ones of both carbon and glass bars. For carbon bars, the global average curve reproduces with good accuracy the experimental results (Figure 12b), while for glass bars, due to the larger scatter of the experimental results, the fit is less accurate.

4.3 **The strain distribution**

The distribution of tensile strain in FRP reinforcement externally bonded to concrete elements depends on the Young's modulus of the FRP reinforcement, E_f: The effective transfer length, L_e, indeed, is directly proportional to E_f (Chen and Teng [26]; fib bulletin 14 [3]). This means that as lower is the value of E_f, the more strains are concentrated close to the loaded end, leading to a smaller L_e. Consequently, smaller volumes of concrete are involved in the debonding failure along the interface. Moreover, since shear bond stresses are related to the gradient of tensile strains along the FRP reinforcement, lower values of E_f also lead to higher shear stresses in the first part of the bonded length. This phenomenon, well known for externally bonded FRP plates and sheets externally, was also observed for the NSM systems tested in Program 1 and characterised by different values of E_f (Bilotta et al. [15]).

For the carbon strips tested in Program 1 (i.e., specimen C-2.5x15-S-2) the experimental and theoretical distributions of tensile strains in the strips and bond shear stresses along the concrete–epoxy interface at several load levels (15, 35 and 55 kN, corresponding to approximately 30, 65, and 100% of the maximum load, respectively) are represented in Figures 13a–b, where '*exp*' and '*num*' indicate curves derived from experimental data and from numerical simulation, respectively. The curves of strains (Figure 13a) clearly show that the FE model is able to reproduce the experimental results for each load level very well. In contrast, for bond stresses, the fit is not as good (Figure 13b). Note that the experimental shear stresses are calculated from the experimental readings from two consecutive strain gauges and their accuracy could be improved by employing a greater number of strain gauges along the reinforcement to reduce the spacing across which the stresses are assumed to be constant. However, using too many strain gauges could alter the bond conditions of the reinforcement, preventing a characterization of the bond conditions representative of NSM-strengthened element (Seracino et al. [14]). The spacing chosen for the tests of Program 1 (70 mm) is considered a reasonable compromise to limit the influence of the strain gauges on the bond mechanisms and to obtain reliable local measures of the bond shear stresses.

Furthermore, Figure 13c and 13d compare the experimental and the numerical distributions of strains and shear stresses, respectively, for a specimen with the 8 mm diameter carbon bar. The good agreement obtained for the strain distributions and the poorer predictive performance for the shear bond stresses is confirmed again and are in general typical of all the simulations conducted in this study.

4.4 **Effect of the bonded length**

For the specimens where 8 mm diameter bars were installed, an investigation of the influence of bond length on the global strength of the NSM bar systems was conducted using the FE model. A bond length of 400 mm was studied in addition to the value of 300 mm used in the experimental tests.

Figure 14 illustrates the numerical *F–d* curves for the specimens C-8-S-2, G-8-RB-3 and B-8-SC-2 for two values of bond length (L_b= 300 and 400 mm). Note that the initial stiffness of the curves, clearly, does not change with bond length, while the maximum load increases notably for the glass and carbon bars and remains constant for the basalt bars. These results indicate that a bond length of 300 mm is not sufficient to transfer the maximum load in the case of the glass and carbon bars; thus the theoretical effective length, corresponding to the full transfer of the maximum pull-out load, is larger than the one adopted in this experimental program (300 mm). By contrast, for the basalt bars the effective length can be estimated about 300 mm. This can be justified by the high axial stiffness of carbon bars and the ribbed surface of the glass bars compared with the basalt ones. As discussed previously, the basalt fibres have an E_f that is similar to that of the glass bars, but the bars are only sand-coated and this could lead to develop a lower effective bond length.

In Figure 15, the bond laws of the 8 mm diameter bars are compared for the bond lengths of 300 and 400 mm. The values of the parameters identifying the bond laws are the same as those listed in Table 3, with the exception of the ultimate slip s_{ult} that is defined after the numerical simulation is run because is related to the failure condition. Thus, about the local behaviour the increase in bond length only determined an increase in s_{ult}.

Table 5 quantifies the effects of the larger L_b for each NSM system. The values of s_{ult}, d_{max} and F_{max} are listed for each series. The initial stiffness of the F–d curve, k^* (assuming a linear branch up to F = 15 kN), is also reported and, as mentioned previously, it remains unchanged when L_b increases. The increase in bond length significantly increases s_{ult} in the local bond law (+58-68%) and d_{max} (+52-80%) in the global behaviour for all types of NSM systems, as evidenced in Figures 14 and 15 too. In contrast, F_{max}, increased markedly for the L_b for the carbon and glass bars only (approximately +23%, on average), while for the basalt bar the change was negligible (+2%). For the basalt bars, indeed, the bond law for the case of L_b = 300 mm was already characterised by a large ultimate slip (approximately 2.6 mm) with a negligible residual shear stress (approximately 0.2 MPa). Thus, the further increase in bond length determined a significant increase of the ultimate slip (4.1 mm) that does not, however, appreciably influence the ultimate load because the residual shear stress is almost zero.

4.5 **Bond behaviour in the transverse plane**

The bond between tensile reinforcement and concrete is essentially a three-dimensional problem. Indeed, the bond law, identified by the interface τ - s relationship, depends on the stress distribution in the surrounding concrete (the radial components of the bond stresses determine tensile stresses in the concrete normal to the reinforcement axis), which can be analysed as a plane strain problem in the plane transverse to the reinforcement. The distribution of the shear bond stresses along the reinforcement is normally determined for a uniaxial condition by solving the differential equation of bond (Sena Cruz et al. [27]).

Using the FE model described previously, the radial components of the bond stresses in the surrounding concrete, σ_{ct}, were obtained for the first bonded finite element closest

to the reinforcement (the loaded end at x = 1.86 mm, Figure 16a) during the entire loading history. Thus, σ_{ct} was calculated by averaging the stress components in the x direction of the four integration points of this element. In Figures 16b-c the distributions of the tangential stress, τ, and the radial stress, σ_{ct}, versus the loaded end slip, s, are depicted for the two types of carbon strips (C-2.5x15-S and C-1.4x10-S).

Figure 17a shows the evolution of the τ/τ_{max} ratio along the normalized bond length, z/L_b, for several load levels, for the C-2.5x15-S strip. The load for which the finite element closest to the loaded end reaches τ_{max} is 62% of the maximum load (F^*=34.60 kN). As the load increases, the τ at the loaded end decreases because the descending branch of the $\tau - s$ law is activated in the first bonded part of the FRP reinforcement. Thus, the maximum shear stress moves in the direction of the free end. When the maximum load is attained (F/F_{max} = 1.0), the bond law is fully developed, which means that at the loaded end the ultimate slip of the $\tau - s$ law, s_{ult}, is reached (see Figure 17c). In Figure 17b, the trend of σ_{ct}/f_{ctm} versus the normalised force, F/F_{max}, is shown for the same finite element, where f_{ctm} is the concrete average compressive strength. Note that the tensile stress in the concrete reaches a maximum when the load is approximately 60% of F_{max}, which is similar to F^*. The σ_{ct}/f_{ctm} ratio exceeds lightly unity because the behaviour of concrete was assumed in the model to be indefinitely linearly elastic. However, the experimental failure mode for this type of strip (Figure 3a) showed that cracks in the concrete actually formed parallel to the load direction.

The distributions along z/L_b of τ/τ_{max} and σ_{ct}/f_{ctm} are shown in Figures 18a and 18b, respectively, for the C-1.4x10-S strip (specimen Lb_70x6) tested in Program 2. For this type of strip, the maximum tensile stress in the concrete surrounding the groove does

not attain the value of f_{ctm}. Thus, cracks do not form in the concrete. This result confirms the observation that the specimens tested by Macedo et al. [20] failed by splitting of the adhesive (see Figure 3b). Note that in this case, the load at which the maximum values of τ/τ_{max} and σ_{ct}/f_{ctm} are reached is approximately 80% of the maximum load (F*=21.73 kN).

Finally, Figure 19a shows the distribution of the radial tensile stress in the concrete, σ_{ct}, along the entire bond length at the load level F^* previously defined for the C-2.5x15-S strip (F*= 0.62 F_{max} =34.60 kN) in the concrete elements close to the reinforcement. In Figure 19b, the same distribution is plotted along the bonded length and for the entire thickness of the concrete block with a colour contour map. At a distance of approximately 50 mm (that is, 20% of L_b) from the loaded end, σ_{ct} becomes negative (i.e., compressive stress) and approaches zero at the free end of the reinforcement. These compressive stresses are evidence of a confinement effect of the concrete surrounding the FRP strip. As Costa and Barros [28] proved, this confinement effect increases with the depth of the strip into the groove, resulting in higher values of F_{max}.

Graphs of the same type are shown in Figures 19 c–d for the C-1.4x10-S strip in specimen Lb-70x6 at F_{max}, which is the load level at which σ_{ct}/f_{ctm} is maximum. The curve shows that σ_{ct} is positive (tensile stress) up to approximately 40% of L_b, and then becomes increasingly negative (compressive stress) up to the free end of the bond length. This trend is different from the one observed in Figures 19a–b for the C-2.5x15-S strip. This may be due to the different loading conditions of the concrete block: in Program 2 (Macedo et al. [20]), the block is loaded in compression, while in Program 1 (Bilotta et al. [15]), the block is loaded in tension.

The distribution of the radial tensile stress in the concrete surrounding the groove, σ_{ct}, was determined for all of the specimens where strips and bars were applied. F^* indicates the load at which both σ_{ct}/f_{ctm} and τ/τ_{max} attain their maximum values. The results are summarised in Table 6 for all types of NSM systems.

For the two carbon systems tested in Program 1 (bars and strips having comparable values of axial stiffness), the tensile strength of the concrete is reached in both cases, but at a lower value of F^* for the bars (28 vs. 35 kN).

Moreover, for the 8-mm-diameter bars tested in Program 1 (smooth carbon, ribbed glass and sand-coated basalt bars), the load F^* decreases if the axial stiffness decreases. In particular, the tensile strength in the concrete is reached (σ_{ct}/f_{ctm} =1) at 27.9 kN for the carbon bars, 20.4 kN for the glass bars, and 18.4 kN for the basalt bars.

Lower values of F^* mean that the tensile strength in the concrete is reached earlier; thus, there is a higher transfer of shear bond stresses along the interfaces that leads to the formation of cracks in the concrete surrounding the NSM reinforcement at lower loads. Therefore, referring to the comparison of carbon strips and bars, the lower value of F^* means that for the bars, the elastic branch of the τ - s law should be stiffer. Indeed, the assessment of the bond parameters by the inverse analysis yielded to estimate a value for s_{max} of approximately 0.10 mm for the carbon bars and approximately 0.33 mm for the strips, while the values of τ_{max} are comparable for the two systems. These values determine a stiffer elastic branch in the bond law of the bars and, as previously observed in section 4.2, the differences in the bond laws depend on the different shape factor of the two systems.

Moreover, referring to the comparison of the 8-mm-diameter bars, the values of F^* show that decreasing the axial stiffness of the NSM system increases the bond transfer,

which is in agreement with the trends in the experimental distributions of strains discussed in section 4.3. Indeed, the gradient of strain distribution near the loaded end increases when the axial stiffness of the reinforcement decreases. A higher gradient means a higher bond stress transfer and, consequently, higher tensile stresses transferred to the surrounding concrete.

Finally, it is interesting to notice that for the 6-mm-diameter basalt bars, the concrete tensile strength is never reached (σ_{ct} = 0.85 f_{ctm}), while for the 8-mm-diameter basalt bars the maximum tensile stress in the concrete increases until it exceeds the strength ($1.28 \cdot f_{ctm}$) at a load of 23.5 kN. This is an unrealistic result because concrete in tension is assumed indefinitely elastic in the model, but it is however significant since leads to suppose that using bars of smaller diameter prevents concrete cracking because the shear stresses along smaller lateral surfaces contribute to do not exceeding the tensile strength of the concrete. However, this conclusion confirms what generally occurs also in concrete elements reinforced with internal steel re-bars: to reduce the risk of concrete spalling, it is better to use more bars of smaller diameter than fewer bars of greater diameter. However, this can be clearly disadvantageous in terms of costs.

5. Conclusions

The FE modelling approach applied in this study to analysis of NSM strengthening systems appears to be well suited to derivation of the values of the significant parameters that define the bond law by inverse analysis. The results of this calibration demonstrate the appropriateness of the selected shape of the $\tau - s$ relationship in terms of simulating the global behaviour of the strengthened element.

The features of the FE model make it possible to analyse and compare the behaviour of the various types of FRP NSM systems tested in two different experimental programs mainly in terms of maximum shear stress, ultimate slip, bond length, and stress field in the concrete. The following conclusions are drawn based on the results of several parametric numerical analyses:

- The parameter that most affects the maximum pullout force, F_{max}, is the bond strength, τ_{max}: i.e., an eightfold increase in τ_{max} corresponds to a fivefold increase in F_{max}.
- Glass bars can support a larger pullout force than basalt bars, even though they two are not much different in terms of Young's modulus. This might be due to the surface treatment of the glass bars (ribs made of epoxy resin vs. sand-coating).
- Smooth carbon bars, with no surface treatment, developed a bond law similar to that of glass bars, even though the ultimate slip was significantly smaller.
- In terms of local behaviour, τ_{max} decreases with increasing E_f, and s_{ult} increases with decreasing E_f.
- In terms of global behaviour, for bars of equal diameter an increase in E_f results in an increase in both the maximum pullout force, F_{max}, and the initial stiffness of the F–d curves, as well as a smaller ultimate displacement.
- Compared with the $\tau - s$ relationships of the carbon bars of similar E_f and smooth surface, the carbon strips were found to develop larger s_{max} and s_{ult}, leading to a more ductile global response in terms of F–d. This can be explained by the larger bond perimeter and the higher confinement provided by the surrounding concrete in the case of the strips.

- Because the values of the bond parameters of carbon and glass bars are not very different, an average bond law has been identified that is capable of predicting fairly well the global pullout behaviour for either type of reinforcement.
- The agreement of the theoretical and experimental results was satisfactory for the strain distributions and less satisfactory for the shear bond stresses, primarily because of the uncertainties associated with the experimental measurement of the latter.
- An increase in bond length from 300 to 400 mm increases s_{ult} in local behaviour and, thus, d_{max} in global behaviour. This results in a +23% increase in F_{max} for the carbon and glass bars. For the basalt bar, however, the load increase is negligible because the ultimate slip corresponding to L_b = 300 mm was already characterised by a very low residual shear stress. This allowed to estimate the effective bond length as about 300 mm for the basalt bars and larger than 300 mm for the carbon and glass bars.
- The distribution of the tensile stresses in the concrete surrounding the NSM reinforcement confirmed the experimental failure mode of the strip tested in Program 2 (splitting of the adhesive) and of strips and bars tested in Program 1 (cracks in the concrete parallel to the load direction).
- The tensile stresses in the concrete along the bond length approached zero at the free end of the reinforcement in the specimens tested in Program 1 (with the concrete block loaded in tension), and became compressive stresses for the specimens tested in Program 2 (with the concrete block loaded in compression).
- The load at crack initiation (i.e., the value corresponding to the condition $\sigma_{ct}=f_{ctm}$) decreases if the axial stiffness decreases and when carbon bars are used instead of strips having similar axial stiffness. This decrease is indicative of a higher transfer of shear bond stresses along the interfaces, which leads to cracking in the concrete

surrounding the NSM reinforcement at lower loads. In terms of local bond law, this means a stiffer elastic branch and/or higher bond strength.

- For bars made of the same material and having the same surface treatment, using a greater number of bars of smaller diameter confirms a low risk of concrete spalling, as well known for concrete elements reinforced with internal steel bars.

Acknowledgements

The experimental activities of Program 1 described in this paper were developed within the research work of the "*European Network for Composite Reinforcement - TR 9.3*".

The research conducted is part of the FCT PreLami project PTDC/ECM/114945/2009.

References

[1] Canadian Standards Association International (CSA). Canadian Highway Bridge design code, *CSA-S6-00,* Toronto.

[2] JSCE. Recommendation for the Upgrading of Concrete Structures with use of Continuous Fiber Sheets. In: *Concrete Engineering Series* No. 41, Japanese Society of Civil Engineers, Tokyo, 250 pp. (available in English).

[3] CEB-FIB. Externally bonded FRP reinforcement for RC structures, *International Federation for Structural Concrete - Technical report,* July 2001, 130 pp.

[4] CNR (National Research Council). Guide for the Design and Construction of Externally Bonded FRP Systems for Strengthening Existing Structures, Advisory Committee on Technical Recommendation for Construction of National Research council, Rome, Italy, pp. 154.

[5] ACI-440. Guide for design and construction of externally bonded FRP systems for strengthening concrete structures, *ACI Technical Report,* May 2002, 118 pp.

[6] Smith, S.T., Teng, J.G. FRP-strengthened RC beams-I: review of debonding strength models. In: *Engineering Structures*, 24 (4), pp. 385–95, 2002.

[7] Ceroni, F., Pecce, M. Statistical analysis of debonding load in concrete elements externally strengthened with CFRP materials. In: Advances in Structural Engineering, 15 (1), pp. 155-168, 2012.

[8] Dias, S.J.E.; Barros, J.A.O. Performance of reinforced concrete T beams strengthened in shear with NSM CFRP laminates. In: *Engineering Structures Journal*, 32 (2), pp. 373-384, 2010.

[9] De Lorenzis, L., Nanni, A. Shear strengthening of reinforced concrete beams with near-surface mounted fiber reinforced polymer rods. In: *ACI Structural Journal,* 98 (1), pp. 60-68, 2001.

[10] Blaschko, M., Zilch, K. Rehabilitation of concrete structures with CFRP strips glued into slits. In: *Proceeding of the 12th International Conference on Composite Materials,* Paris, France, 1999.

[11] De Lorenzis, L., Teng, J.C. Near-surface mounted FRP reinforcement: An emerging technique for strengthening structures. In: *Composites Part B: Engineering,* 38, pp. 119-43, 2007.

[12] Sena Cruz, J.M., Barros, J.A.O. Bond Between Near-Surface Mounted Carbon-Fiber-Reinforced Polymers Laminate Strips and Concrete. In: *ASCE Journal of Composite for Construction,* 8 (6), pp. 519-527, 2004.

[13] Hassan, T., Rizkalla, S., (2003). "Investigation of bond in concrete structures strengthened with near surface mounted carbon fiber reinforced polymer strips", *ASCE Journal of Composites for Construction,* 7 (3), pp. 248-257.

[14] Seracino, R., Jones, N.M., Page, M.W., Ali, M.S.S., Oehlers, D.J. Bond strength of near-surface mounted FRP-to-concrete joints. In: *ASCE Journal of Composites for Construction*, 11 (4), pp. 401-409, 2007.

[15] Bilotta, A., Ceroni, F., Di Ludovico, M., Nigro, E., Pecce, M., Manfredi, G. Bond efficiency of EBR and NSM FRP systems for strengthening of concrete members. In:

ASCE Journal of Composites for Construction, doi: 10.1061/(ASCE)CC.1943-5614.0000204, 2011.

[16] Novidis, D.G., Pantazopoulou, S.J. Bond test of short NSM-FRP and steel bar anchorage. In: *ASCE Journal of Composites for Construction*, 12 (3), pp. 323-333, 2008.

[17] Borchert, K., Zilch H. Bond behaviour of NSM FRP strips in service, Structural Concrete. In: *Thomas Telford and fib journal*, pp. 1464–4177, 2008.

[18] En-Core & fib TG 9.3. *Internal reports: Round Robin Testing Exercise* - Universities of Gent, Minho and Budapest available on http://cigroup.shef.ac.uk/encore/rrt/index.php, 2011.

[19] Sena-Cruz, J.M., Barros, J.A.O., Azevedo, A.F.M., Ventura-Gouveia, A. Numerical simulation of the nonlinear behavior of RC beams strengthened with NSM CFRP strips. In: *Proc. of CMNE 2007 - Congress on Numerical Methods in Engineering and XXVIII CILAMCE - Iberian Latin American Congress on Computational Methods in Engineering*, paper nº 485 published in CD – FEUP, 20 pp., Porto, 13-15 June 2007.

[20] Macedo, L., Costa, I.G., Barros, J.A.O. Evaluation of influence of adhesive and geometry of laminated carbon fiber on the behavior of startup tests. In: *Proc. of Structural Concrete 2008,* Guimarães, Portugal, 2008 [in Portuguese].

[21] Eurocode 2. Design of Concrete structures – Part 1-1: General Rules and Rules for Buildings, ENV 1992-1-1: 2004: E.

[22] Ceroni, F., Bilotta, A., Nigro, E, Pecce, M. Bond behaviour of FRP NSM systems in concrete elements, *Composites: Part B,* 43, pp. 99–109, 2012.

[23] Ianniciello, M. Modeling of bond behavior in RC elements externally bonded with NSM FRP systems. *Master Thesis in Structural Engineering*, University of Sannio, Benevento, Italy, 197 pp., 2011

[24] Eligehausen R., Popov E.P., Bertero V.V. Local Bond Stress-Slip Relationships of Deformed Bars Under Generalized Excitations. In: *Report n° 83/23*, EERC, University of California, Berkeley, 1983.

[25] Barros, J.A.O.; Kotynia, R. Possibilities and challenges of NSM for the flexural strengthening of RC structures. In: Proc. of Fourth International Conference on FRP Composites in Civil Engineering (CICE2008), Zurich, Switzerland, 22-24July 2008.

[26] Chen, J.F., Teng, J.G. Anchorage strength models for FRP and Steel Plates bonded to concrete. In: *Journal of Structural Engineering*, 127 (7), pp. 784-791, 2001.

[27] Sena-Cruz, J.M., Barros, J.A.O., Gettu, R., Azevedo, A.F.M. Bond Behavior of Near-Surface Mounted CFRP Laminate Strips under Monotonic and Cyclic Loading. In: *ASCE Journal of Composites for Construction*, 10 (4), pp. 295-303, 2006.

[28] Costa, I.G., Barros, J.A.O. Assessment of the bond behavior of NSM FRP materials by pullout tests. In: *Proc. of First Middle East Conference on Smart Monitoring, Assessment and Rehabilitation of Civil Structures*, Dubai, 8-10 February 2011.

List of Table

List of Figures

Figure 14. Comparison between the numerical *F–d* curves for smooth carbon, ribbed glass and sand-coated basalt bars for bond lengths of 300 and 400 mm.

Figure 15. Comparison between the numerical τ–*s* curves for smooth carbon, ribbed glass and sand-coated basalt bars for bond lengths of 300 and 400 mm.

Figure 16. a) Scheme for the calculation of tensile stress in the concrete in the transverse plane; Distribution of bond shear stresses and tensile stress in the concrete at the loaded end: b) C-2.5x15-S carbon strip tested in Program 1; c) C-1.4x10-S carbon strip tested in Program 2.

Figure 17. Specimen C-2.5x15-S: a) Theoretical distribution of normalised shear bond stresses along the bond length for different load levels; b) Theoretical distribution of normalised tensile stresses in the concrete; c) Qualitative τ–s laws for the loaded and free ends.

Figure 18. C-1.4x10-S strip in specimen Lb_70x6: a) Theoretical distribution of normalised shear bond stresses along the bond length for different load levels; b) Theoretical distribution of normalised tensile stresses in the concrete.

Figure 19. Distribution of σ_{ct} along the bond length at F = 0.62 F_{max}: a) specimen C-2.5x15-S-2; b) C-1.4x10-S strip in specimen Lb_70x6.

Table 1. Main experimental data and results for Program 1

Specimen	f_{fu} [MPa]	E_f [GPa]	$E_f A_f$ [kN]	k [-]	Failure mode[(a)]	F_{max} [kN]	d_{max} [mm]
B-6-SC-1	1282	46	1300	1.67	E/C	33.87	2.93
B-6-SC-2					E/C	28.84	2.37
B-8-SC-1	1272	46	2311	1.75	E/C	31.57	1.08
B-8-SC-2					E/C	33.10	0.86
B-8-SC-3					E/C	30.24	1.45
G-8-RB-1	1333	59	2964	1.75	E/C	46.71	2.50
G-8-RB-2					E/C	45.25	1.51
G-8-RB-3					E/C	50.86	2.15
C-8-S-1	2495	155	7787	1.75	E/C+CL	48.52	0.88
C-8-S-2					E/C+CL	55.30	1.10
C-8-S-3					E/C+CL	45.23	0.84
C-2.5x15-S-1	2863	182	6825	1.67	E/C	52.97	1.32
C-2.5x15-S-2					E/C	56.03	1.28
C-2.5x15-S-3					E/C	46.26	1.24

[(a)] E/C: debonding at the epoxy-concrete interface, CL: detachment of a concrete layer

Table 2. Main experimental data and results for Program 2

Specimen	f_{fu} [MPa]	E_f [GPa]	$E_f A_f$ [kN]	k [-]	Failure mode[(a)]	F_{max} [kN]	d_{max} [mm]
Lb40_x6	2879	156	2184	2.20	S	18.59	0.60
Lb40_x12					S	19.90	0.41
Lb70_x6	2879	156	2184	2.20	S	27.69	0.68
Lb70_x12					S	31.43	0.64
Lb90_x6	2879	156	2184	2.20	S	33.90	0.92
Lb90_x12					S	35.63	0.82
Lb120_x6	2879	156	2184	2.20	S	34.46	0.72
Lb120_x12					S	37.92	0.79
Lb150_x6	2879	156	2184	2.20	S	36.43	1.03
Lb150_x12					S	38.35	0.85

[(a)] S: Splitting of adhesive

Table 3. Values of the bond law parameters assessed by inverse analysis

Experimental program	*Specimen*	E_f [GPa]	s_{lin} [mm]	s_{max} [mm]	τ_{max} [MPa]	α [-]	α' [-]	s_{ult} [mm]	$F_{max,num}$ [kN]	$F_{max,exp}$ [kN]
Program 1	B-6-SC	46	0.05	0.41	7.09	0.40	0.65	2.30	29.21	29.17
	B-8-SC	46	0.05	0.43	7.63	0.40	1.93	2.51	31.67	31.59
	G-8-RB	59	0.01	0.08	6.50	0.40	0.32	2.42	45.01	47.06
	C-8-S	155	0.01	0.10	5.73	0.40	0.31	0.92	50.62	49.61
	C-2.5x15-S	159	0.05	0.33	5.26	0.35	1.13	1.32	52.05	51.75
Program 2	Lb70_x6	156	0.05	0.40	17.35*	0.40	0.40	0.84	27.27	27.69
	Lb90_x6	156	0.05	0.40	16.52*	0.40	0.40	1.11	33.50	33.90

* shear stresses referred to the strip-epoxy interface

Table 4. Numerical results of the specimens with 8 mm diameter glass and carbon bars in Program 1

Specimens	$\mathbf{E_f}$	$\mathbf{s_{lin}}$	$\mathbf{s_{max}}$	$\boldsymbol{\tau_{max}}$	$\boldsymbol{\alpha}$	$\boldsymbol{\alpha'}$	$\mathbf{s_{ult}}$	$\mathbf{G_f}$	$\mathbf{d_{max}}$	$\mathbf{F_{max}}$
	[GPa]	[mm]	[mm]	[MPa]	[-]	[-]	[mm]	[N/mm]	[mm]	[kN]
C-8-S	155.0	**0.01**	**0.10**	**5.73**	**0.40**	**0.31**	**0.92**	**3.56**	**1.11**	**50.62**
G-8-RB	59.0	**0.01**	**0.08**	**6.50**	**0.40**	**0.32**	**2.42**	**7.79**	**2.50**	**45.01**
Global average		0.01	0.09	6.12	0.40	0.31	---	---	---	---
CoV (%)		*0.0*	*15.7*	*8.9*	*0.0*	*2.2*	---	---	---	---

Table 5. Evaluation of the influence of L_b on the bond behaviour of the 8-mm-diameter bars

Specimen	$\mathbf{K^*}$	$\mathbf{L_b}$	$\mathbf{s_{ult}}$	$\boldsymbol{\Delta s_{ult}}$	$\boldsymbol{\Delta G_f}$	$\mathbf{d_{max}}$	$\mathbf{F_{max}}$	$\boldsymbol{\Delta d_{max}}$	$\boldsymbol{\Delta F_{max}}$
	[kN/mm]	[mm]	[mm]	[%]	[%]	[mm]	[kN]	[%]	[%]
C-8-S-2	190.5	300	0.98	---	---	1.21	55.89	---	---
		400	1.65	68	54	1.94	68.07	+60	+22
G-8-RB-3	106.4	300	2.37	---	---	2.55	49.75	---	---
		400	3.87	63	49	4.59	61.95	+80	+25
B-8-SC-2	70.2	300	2.58	---	---	2.72	33.50	---	---
		400	4.07	58	4	4.14	34.15	+52	+2

Table 6. Influence of type of reinforcement on the value of F^*/F_{max}

Type	**Mat.** [(a)]	**Surface** [(b)]	$\mathbf{E_f}$	$\mathbf{d_f}$ [(c)]	$\mathbf{E_fA_f}$	$\boldsymbol{(\sigma_{ct}/f_{ctm})^*}$	$\boldsymbol{\tau_{max}}$	$\boldsymbol{(\tau/\tau_{max})^*}$	$\mathbf{F^*/F_{max}}$	$\mathbf{F_{max}}$	$\mathbf{F^*}$
			[GPa]	[mm]	[kN]	[-]	[MPa]	[-]	[%]	[kN]	[kN]
Bar	C	S	155	8	7787	1.04	6.00	1.0	50	55.9	27.9
Strip	C	S	182	2.5x15	6825	1.03	5.41	1.0	62	55.8	34.6
Bar	G	RB	59	8	2964	1.08	6.50	1.0	41	49.8	20.4
Bar	B	SC	46	8	2311	1.28 1.00	8.23	1.0 0.8	70 55	33.5	23.5 18.4
Bar	B	SC	46	6	1300	0.85	6.84	1.0	50	27.7	13.9
Strip	C	S	156	1.4x10	2184	0.91	8.70	1.0	80	27.2	21.7
	[(a)] *C*: carbon; *G*: glass; *B*: basalt. [(b)] *S*: smooth; *RB*: ribbed; *SC*: sand coated. [(c)] $t_f x\ b_f$ for strips.										

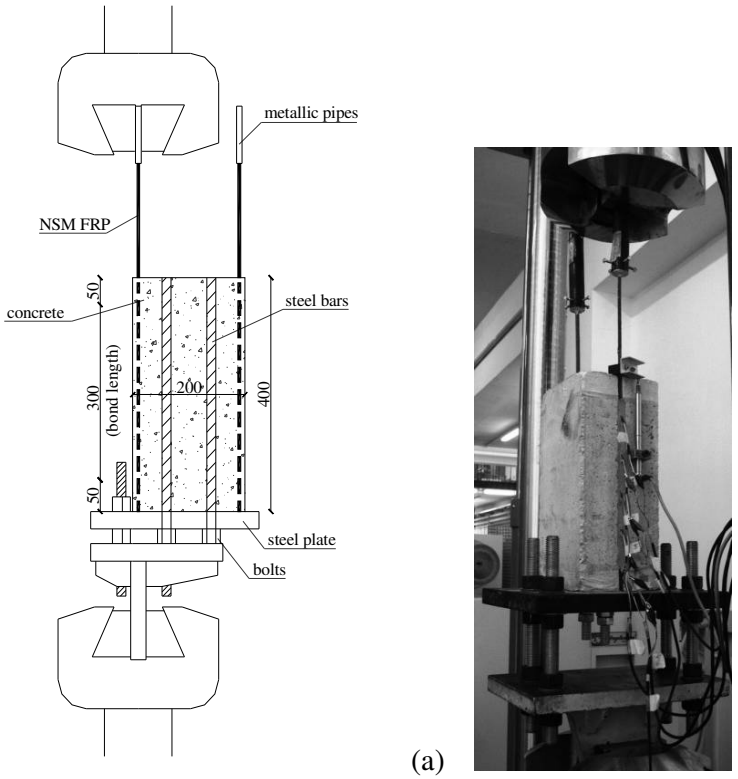

(a) (b)

Figure 1. Test configuration for experimental Program 1 (Bilotta et al. [15]) (dimensions in mm).

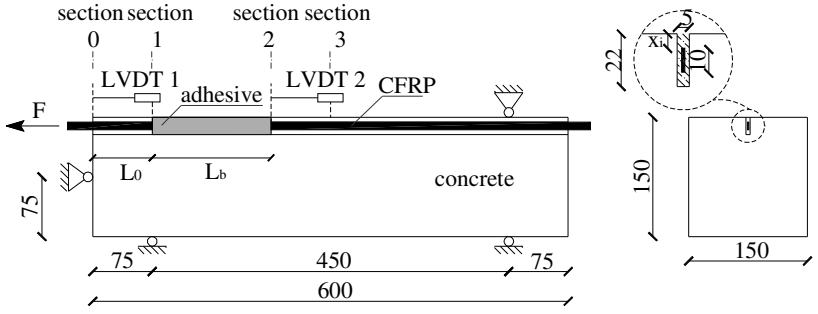

Figure 2. Test configuration of experimental Program 2 (Macedo et al. [20]).

(a)

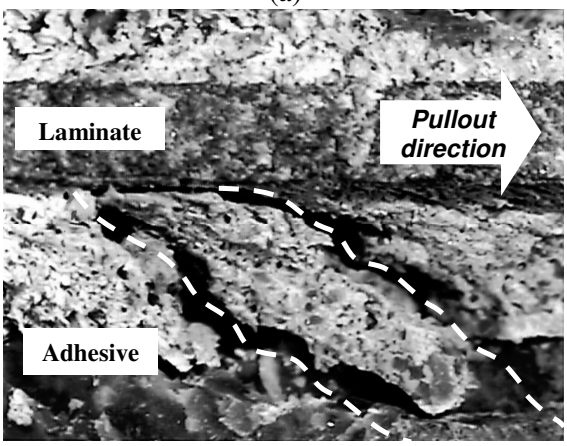

(b)

Figure 3. a) Debonding at the epoxy–concrete interface for specimens of Program 1; b) Splitting of epoxy adhesive for specimens of Program 2.

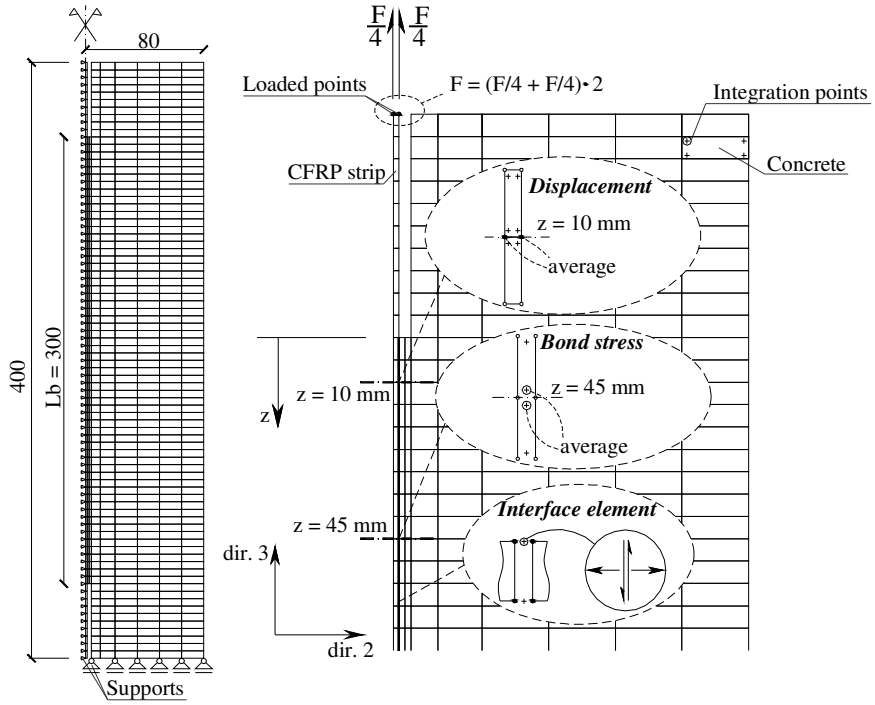

Figure 4. Finite element idealisation of specimens tested in Program 1: (a) complete mesh; (b) detailed diagram of the top side (dimensions in mm).

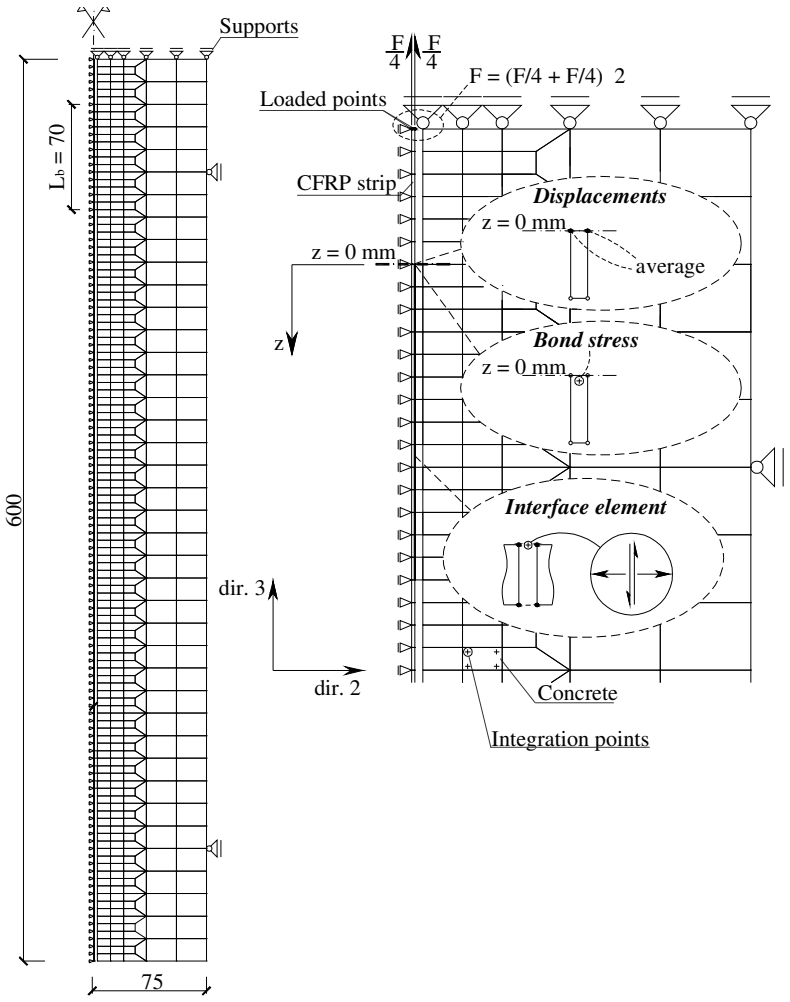

(a) (b)

Figure 5. Finite element idealisation of specimens tested in Program 2: (a) complete mesh; (b) detailed diagram of the top side (dimensions in mm).

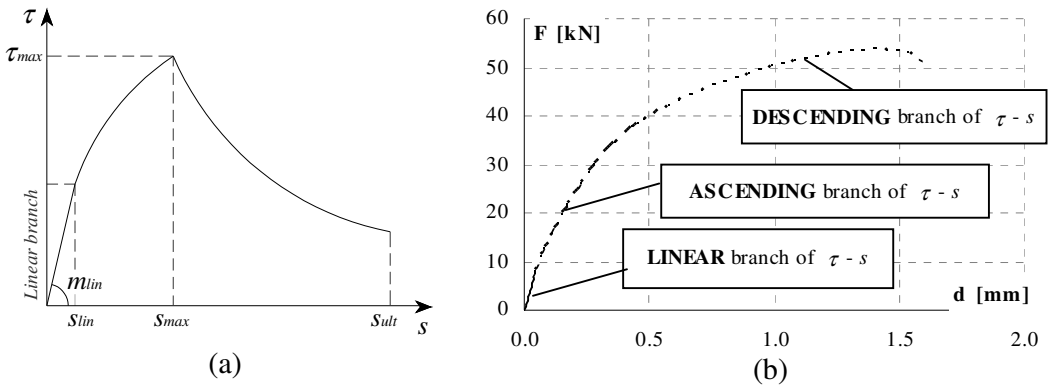

Figure 6. (a) Local bond stress–slip relationship; (b) qualitative correlation between τ-s and F-d relationships in a bond test.

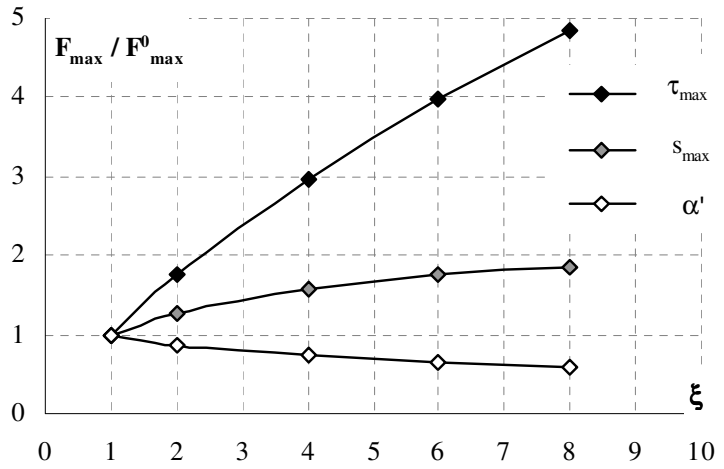

Figure 7. Effect of s_{max}, τ_{max} and α' on the maximum pullout force, F_{max}.

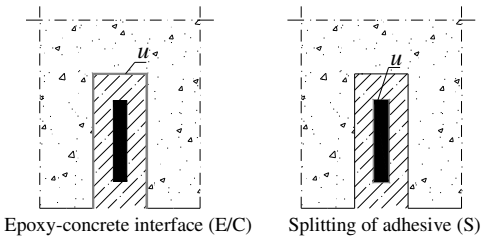

Figure 8. Definition of the perimeter *u* when different failure modes occur.

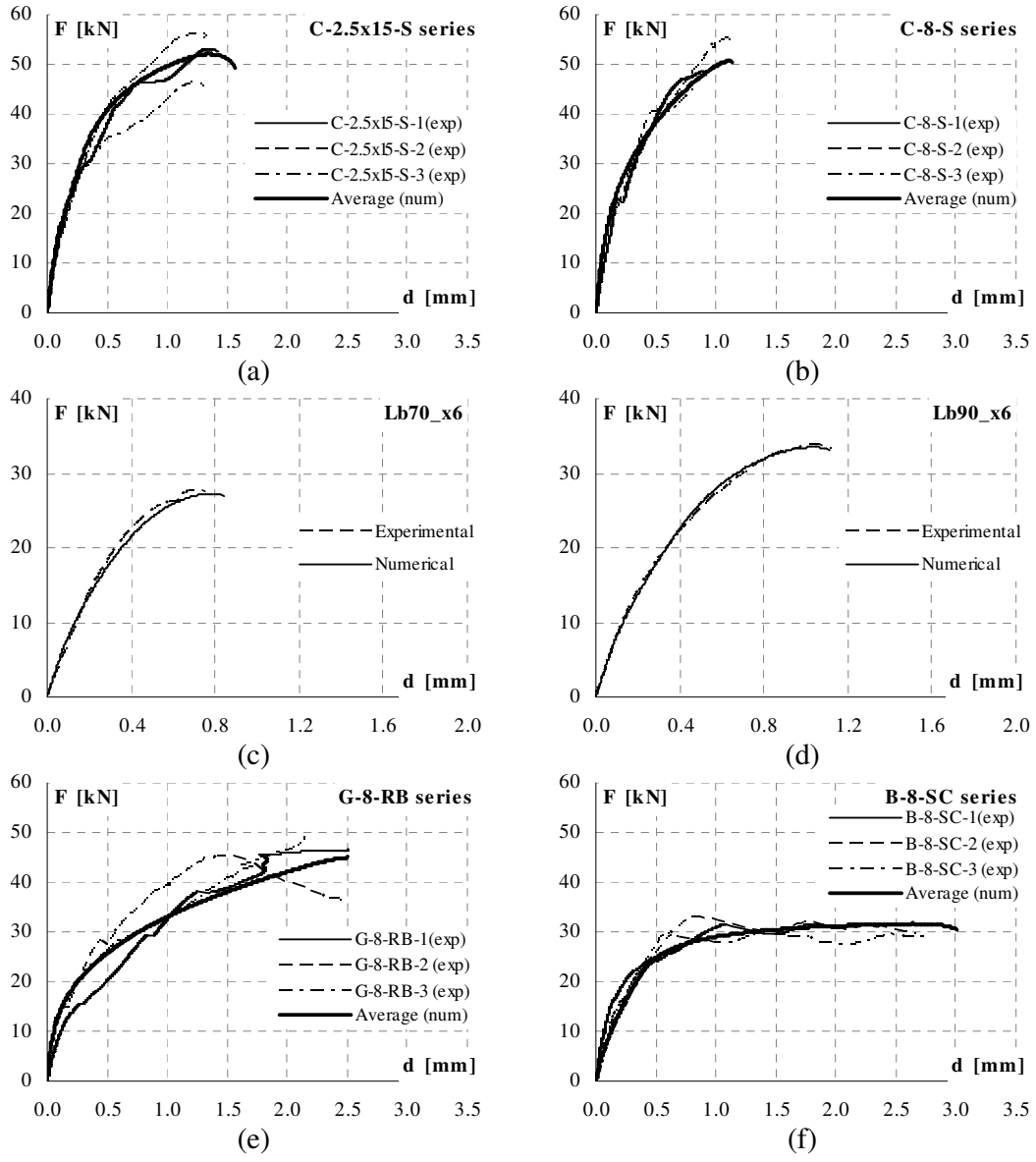

Figure 9. Experimental vs. numerical pullout force–displacement curves for different NSM systems: (a) 2.5 mm×15 mm carbon strips (Program 1); (b) 8 mm diameter carbon bars; (c) 1.4 mm×10 mm carbon strips (Program 2); (d) 1.4 mm×10 mm carbon strips (Program 2); (e) 8 mm diameter ribbed glass bars (Program 1); (f) 8 mm diameter sand coated basalt bars (Program 1).

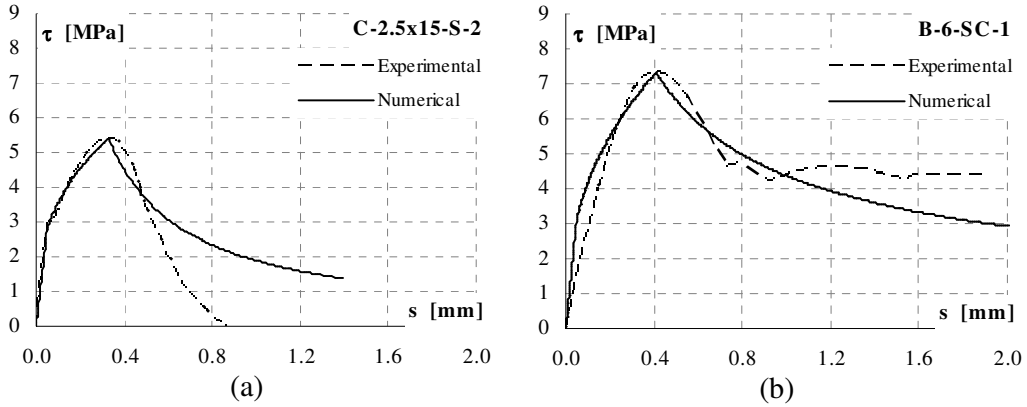

Figure 10. Numerical–experimental comparison of the local bond law for different FRP NSM systems: (a) 2.5 mm×15 mm carbon strips; (b) 6 mm diameter basalt bars.

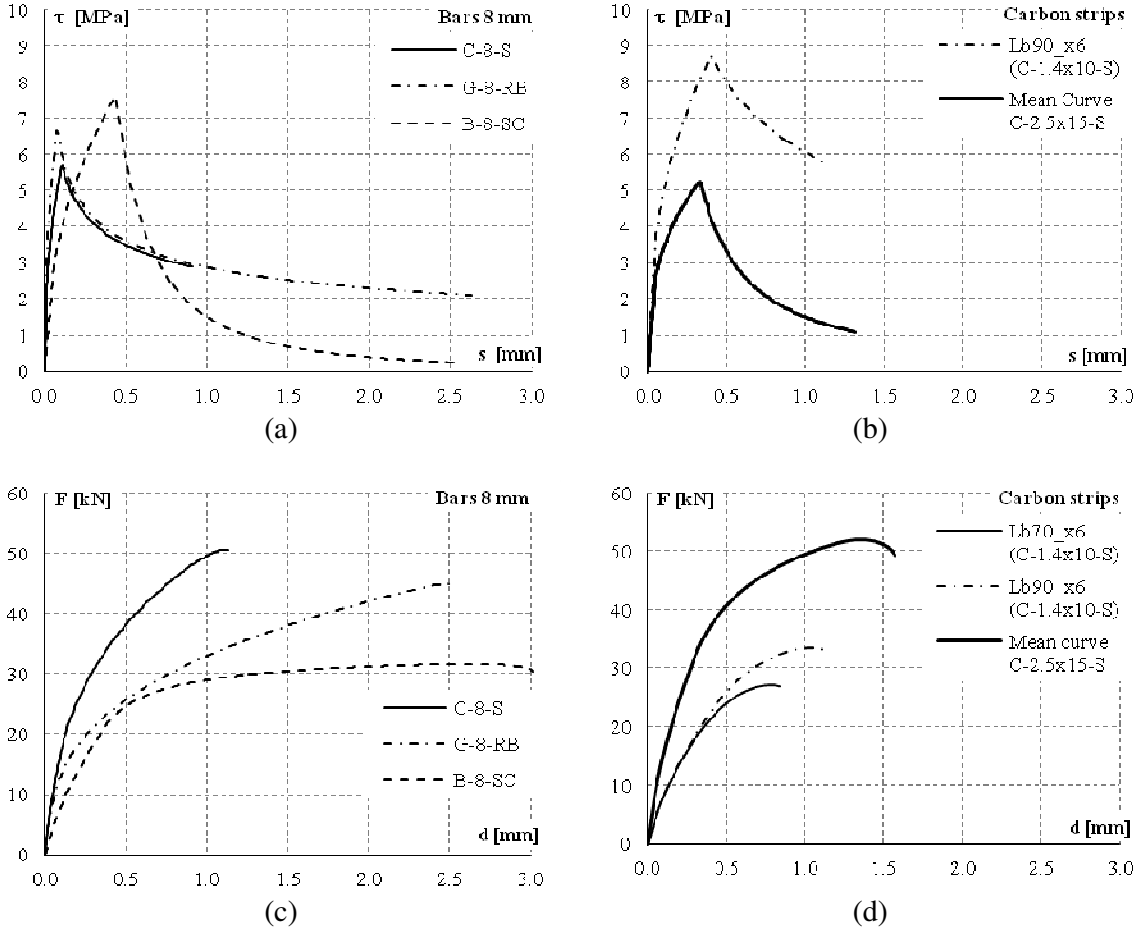

Figure 11. Numerical curves for different types of NSM reinforcements: a) τ- s relationships for 8 mm diameter bars, b) τ - s relationships for carbon strips; c) F–d curves for 8 mm diameter bars; d) F–d curves for carbon strips.

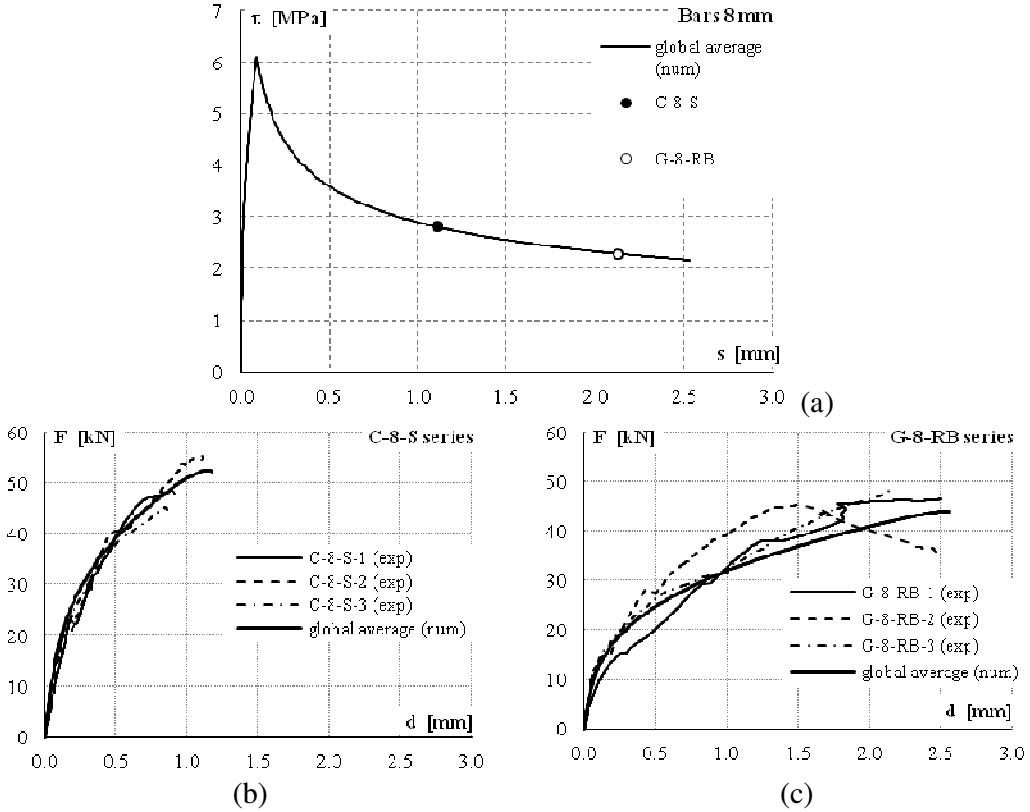

Figure 12. a) Average numerical τ–s curves for the carbon and 8-mm-diameter glass bars. Comparison of experimental and numerical F–d curves for: b) 8-mm-diameter carbon bars and c) 8-mm-diameter glass bars.

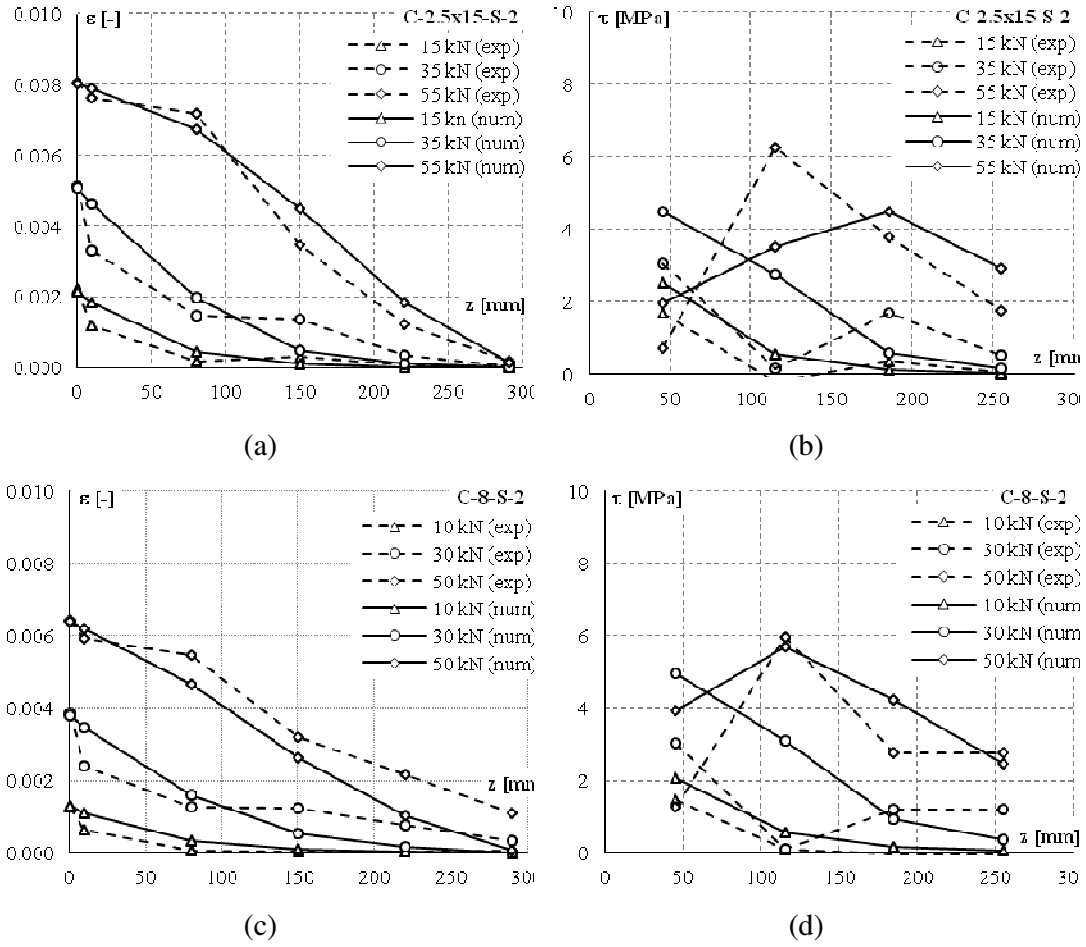

Figure 13. Numerical and experimental comparisons: a) tensile strain and b) bond shear stress distribution for specimen C-2.5x15-S-2; c) tensile strain and d) bond shear stress distribution for specimen C-8-S-2.

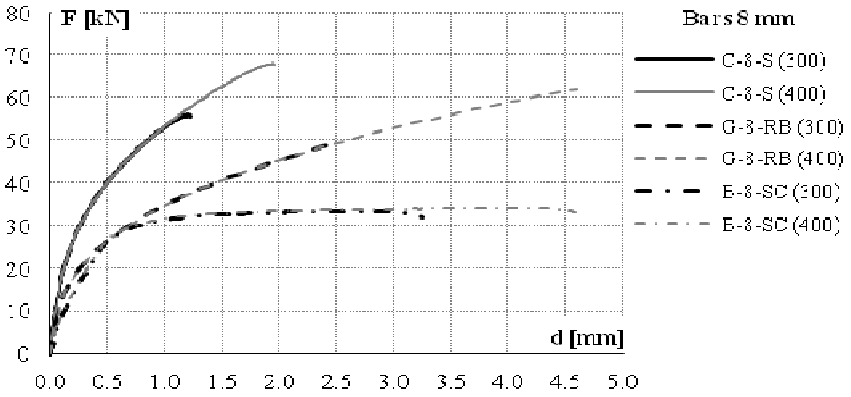

Figure 14. Comparison between the numerical *F–d* curves for smooth carbon, ribbed glass and sand-coated basalt bars for bond lengths of 300 and 400 mm.

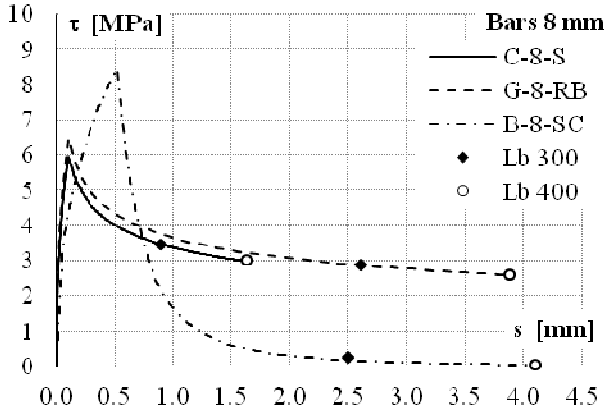

Figure 15. Comparison between the numerical *τ–s* curves for smooth carbon, ribbed glass and sand-coated basalt bars for bond lengths of 300 and 400 mm.

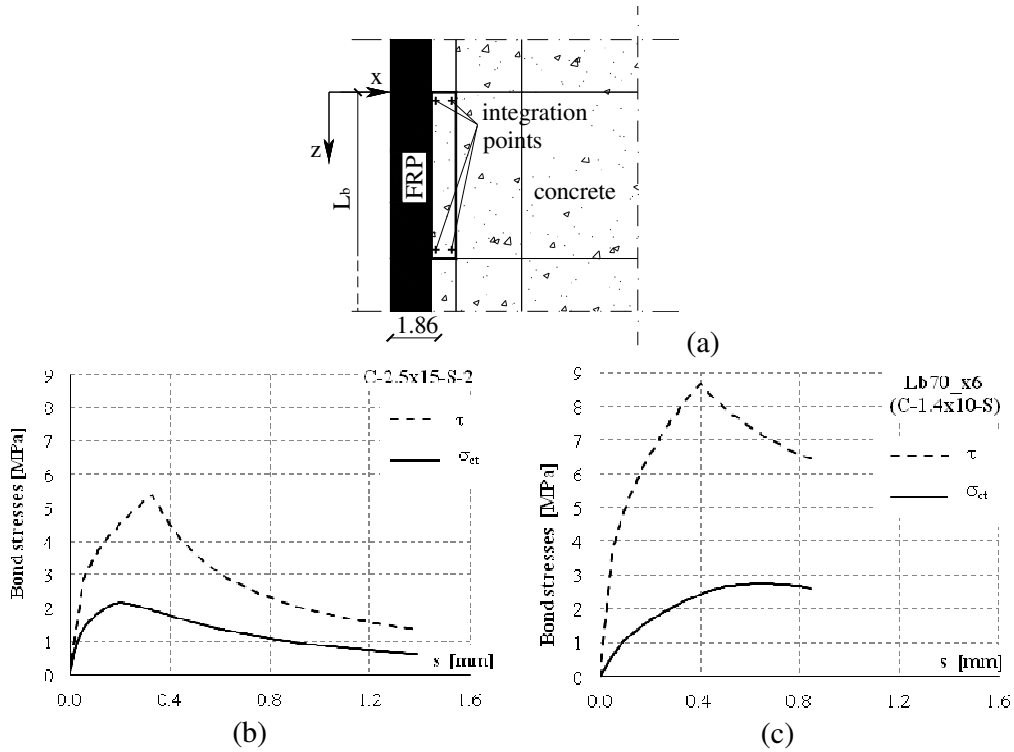

Figure 16. a) Scheme for the calculation of tensile stress in the concrete in the transverse plane; Distribution of bond shear stresses and tensile stress in the concrete at the loaded end: b) C-2.5x15-S carbon strip tested in Program 1; c) C-1.4x10-S carbon strip tested in Program 2.

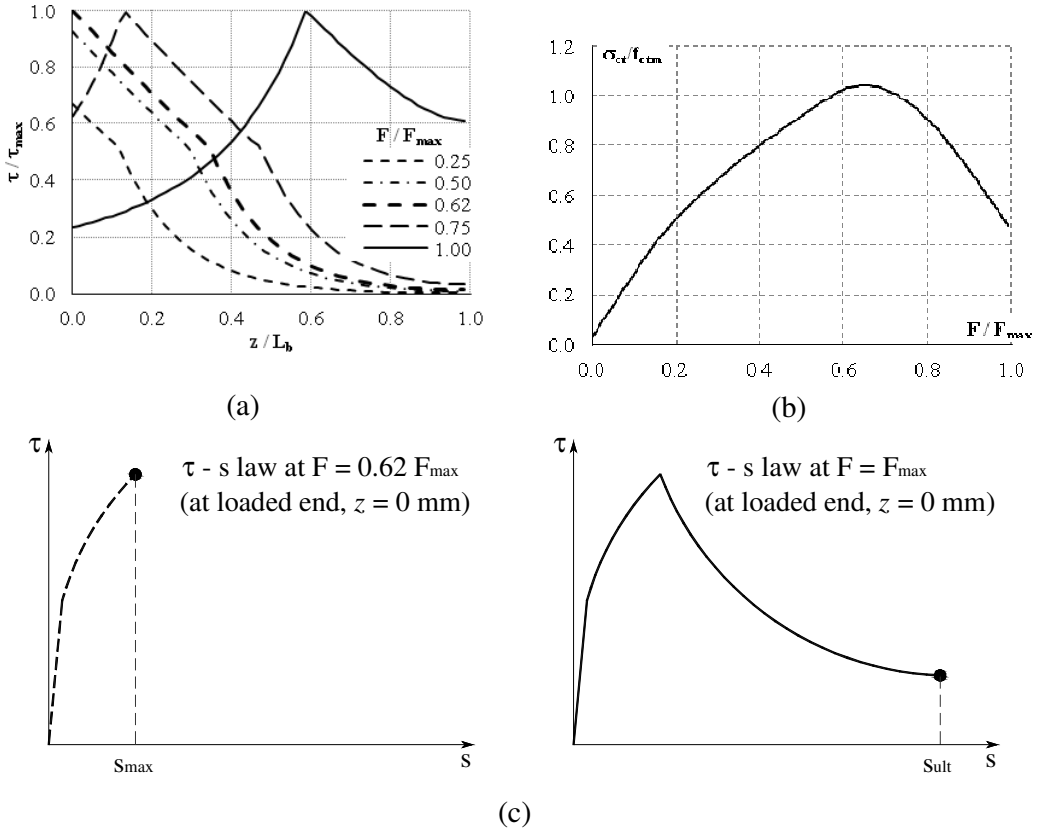

Figure 17. Specimen C-2.5x15-S: a) Theoretical distribution of normalised shear bond stresses along the bond length for different load levels; b) Theoretical distribution of normalised tensile stresses in the concrete; c) Qualitative τ–s laws for the loaded and free ends.

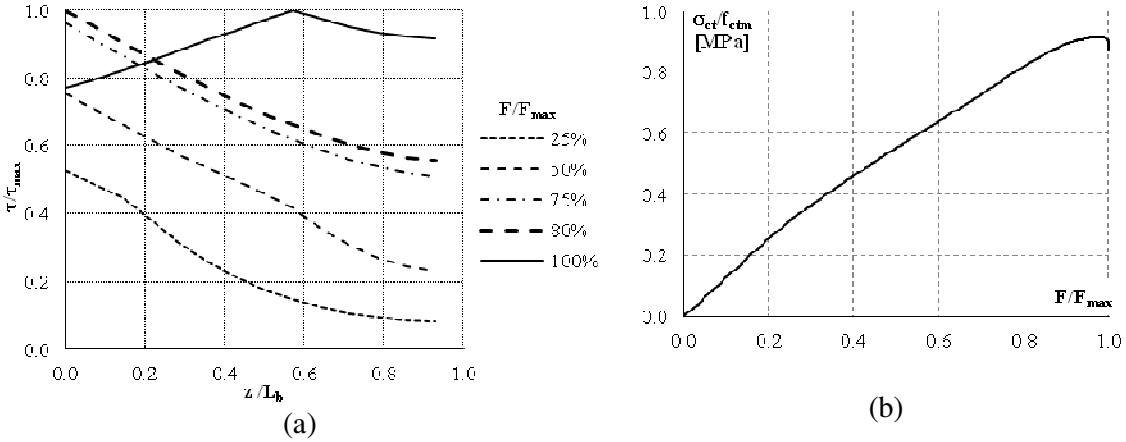

Figure 18. C-1.4x10-S strip in specimen Lb_70x6: a) Theoretical distribution of normalised shear bond stresses along the bond length for different load levels; b) Theoretical distribution of normalised tensile stresses in the concrete.

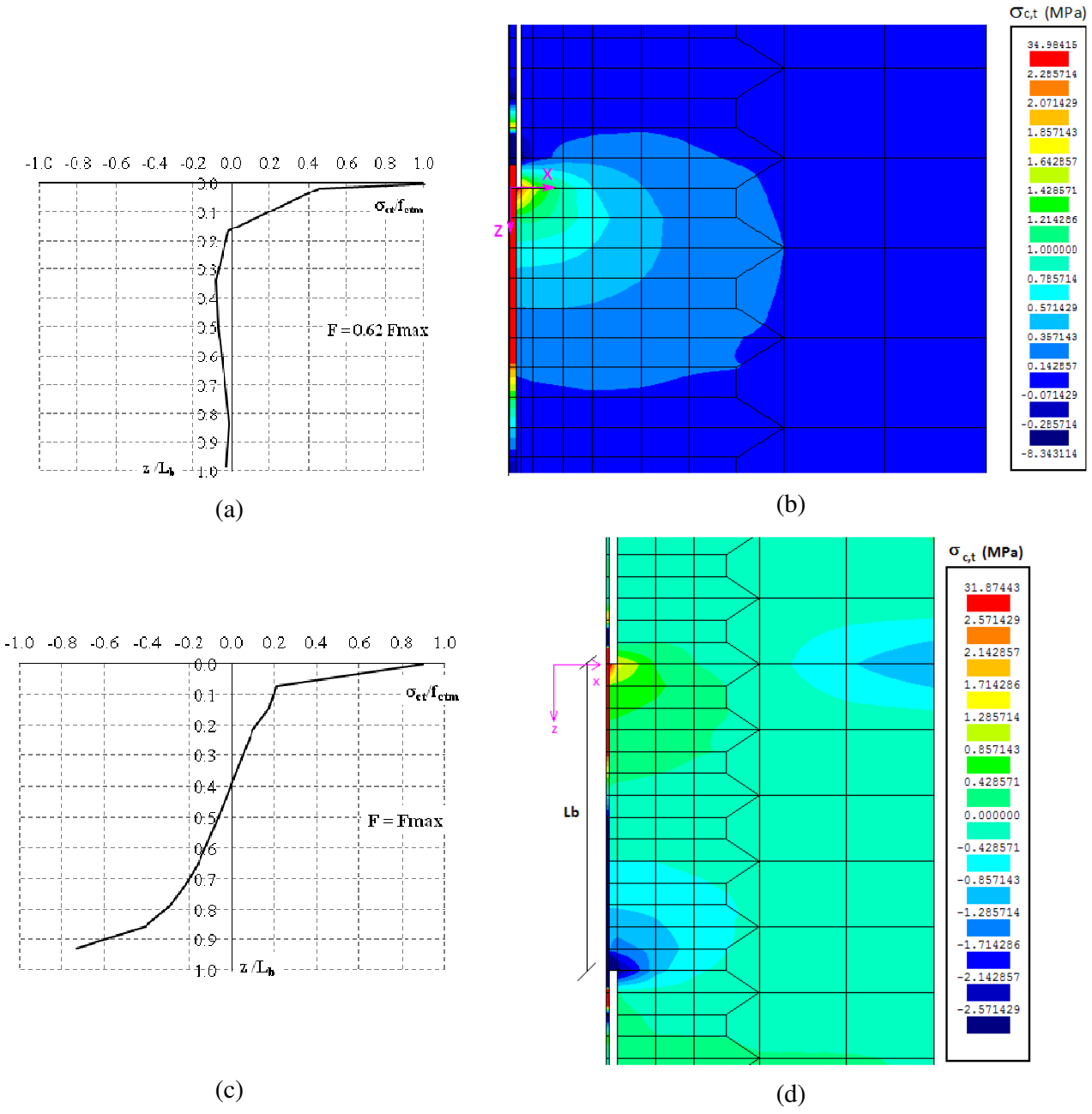

Figure 19. Distribution of σ_{ct} along the bond length at F = 0.62 F_{max}: a) specimen C-2.5x15-S-2; b) C-1.4x10-S strip in specimen Lb_70x6.